

Submitted to Journal of Chemical Physics (2022), in press.

Spin-orbit transitions in the $N^+(^3P_{JA}) + H_2 \rightarrow NH^+(X^2\Pi, ^4\Sigma^-) + H(^2S)$ reaction, using adiabatic and mixed quantum-adiabatic statistical approaches

Susana Gómez-Carrasco*

Facultad de Farmacia, Universidad de Salamanca, Campus Miguel de Unamuno, C. Lic. Méndez Nieto, s/n, 37007-Salamanca, Spain

Daniel Félix-González and Alfredo Aguado

Unidad Asociada UAM-CSIC, Departamento de Química Física Aplicada,
Facultad de Ciencias M-14, Universidad Autónoma de Madrid, 28049, Madrid, Spain

Octavio Roncero†

Instituto de Física Fundamental (IFF-CSIC), C.S.I.C., Serrano 123, 28006 Madrid, Spain

The cross section and rate constants for the title reaction are calculated for all the spin-orbit states of $N^+(^3P_{JA})$ using two statistical approaches, one purely adiabatic and the other one mixing quantum capture for the entrance channel and adiabatic treatment for the products channel. This is made by using a symmetry adapted basis set combining electronic (spin and orbital) and nuclear angular momenta in the reactants channel. To this aim, accurate *ab initio* calculations are performed separately for reactants and products. In the reactants channel, the three lowest electronic states (without spin-orbit couplings) have been diabaticized, and the spin-orbit couplings have been introduced through a model localizing the spin-orbit interactions in the N^+ atom, which yields accurate results as compared to *ab initio* calculations including spin-orbit couplings. For the products, eleven purely adiabatic spin-orbit states have been determined with *ab initio* calculations. The reactive rate constants thus obtained are in very good agreement with the available experimental data for several ortho- H_2 fractions, assuming a thermal initial distribution of spin-orbit states. The rate constants for selected spin-orbit J_A states are obtained, to provide a proper validation of the spin-orbit effects to obtain the experimental rate constants.

I. INTRODUCTION

The formation of hydrides can be considered as the first step of chemistry in space and determines the abundances of more complex molecules arising in chemical networks from them. The study of the evolution of abundances of molecular species allows the probe of physical conditions along the stellar evolution, from the parent molecular cloud to the star system, passing through the intermediate stages such as cold and hot cores, protoplanetary disk, etc. Among the most abundant elements, nitrogen plays a singular role, because its more abundant forms are thought to be N_2 and atomic nitrogen, which are difficult to be observed because they have no permanent dipole moment, specially in cold cores. The abundance of nitrogen is then established by other molecules, such as its hydrides NH_n , CN, HCN/HNC, N_2H^+ , etc, requiring the construction of increasingly more accurate chemical networks [1, 2].

Nitrogen hydrides are particularly interesting and ammonia is among the first polyatomic molecules detected in the interstellar medium (ISM) [3]. The ortho/para ratios observed for NH_2 and NH_3 [4] and their deuteration enrichment [5] serve as sensitive probes to check gas-phase chemistry models [2]. In this regard, hydrides present a comparably small number of reactions in the chemical networks. In photodissociation regions (PDR), hydrides are normally formed from the atoms

(neutral and/or cations, depending on their ionization potential, as compared to atomic hydrogen) by successive addition of hydrogen atoms, followed by dissociative recombination with electrons in the case of cations. The ionization step in nitrogen in PDR is improbable difficult because its ionization energy is larger than that of hydrogen, unlike most of other metal atoms, and the density of N^+ is therefore smaller. Therefore other neutral reactions of N atoms with OH and CH are alternative routes to form nitrogen hydrides [2].

The rate constants involved in the first steps of the chemical networks have an enormous influence in the relative abundances, ortho/para ratios and deuteration fractions of many of the nitrogen-bearing molecules. For these reasons many experiments have been performed to study the following reaction [6–9]:



These experiments are performed in different conditions, which raises questions about the reactivity associated to each fine structure state of $N^+(^3P_{JA})$, since the exact thermalization conditions are not known.

Theoretical dynamical calculations have been performed on the ground adiabatic electronic state potential [10–13], both classical [13, 14] and quantum [15, 16] ones, without taking into account the fine structure of nitrogen. These studies demonstrate that the reaction dynamics in the ground adiabatic state is mediated by many long lived resonances due to the deep insertion well of the potential energy surface (PES). These calculations suggest that the reaction proceeds statistically, but none of them describe any electronic transition among spin-orbit states.

*Electronic address: susana.gomez@usal.es

†Electronic address: octavio.roncero@csic.es

Several statistical simulations have been recently performed including the fine structure [17, 18]. However, in these statistical simulations only long range interactions are included, within the assumption that only the first 3 adiabatic fine-structure states can react. However, the inclusion of transitions among the different spin-orbit states in the entrance channel may include important variations of the experimentally determined rate constants, specially at low temperature, as it has been discussed by Zymak *et al.* [8] and Fanghanel [9].

The main goal of this work is simulating the transitions between the fine structure $N^+(^3P_{J_A})$ states, determining the cross sections and rates for each of them individually. Since the problem involves 9 spin-orbit states, some of them showing deep insertion wells, complete quantum calculations are not feasible. For this reason, in this work a detailed potential model is developed separately for reactants and products, all based on accurate *ab initio* calculations. In the $N^+(^3P_{J_A}) + H_2$ reactants channel, a diabatic model is developed allowing to include the couplings among the spin-orbit states. In the products channel, pure adiabatic spin-orbit potentials are calculated. These diabatic states are used to build total electronic and angular basis sets allowing the study of the correlation of angular momenta, electronic and nuclear, to properly describe spin-orbit transitions[19]. These basis set functions are then used within an adiabatic statistical (AS) approximation [20] and mixed description of the AS and a quantum statistical (QS) [21–24] (denoted by the acronym QAS). The AS approximation has been recently applied to the study of many reactions and inelastic processes for many systems and is widely used[25]. A precedent of mixing quantum capture in the entrance channel and statistical approaches to describe the reaction probability has been proposed previously for four atom complex-forming reactions[26]. In this work, the calculation of quantum capture probabilities is done with a time-independent method based on a renormalized Numerov propagation scheme developed to this aim and presented in the Appendix A.

This work is organized as follows. A detailed *ab initio* study of the system will be described in section II, treating separately reactants, $N^+(^3P_{J_A}) + H_2(X^1\Sigma_g^+)$, and products, $H(^2S) + NH^+(^2\Pi, ^4\Sigma^-)$ channels, including spin-orbit couplings. In the case of the reactants, a diabatic model is built for the different $N^+(^3P_{J_A})$ states, which is necessary to include the transitions among them. The PESs will be used to calculate the capture probabilities needed in the quantum and adiabatic statistical methods, and described in section III, paying special attention to the transitions among different fine structure states. Also cross sections and rate coefficients for each individual state will be presented in section IV. Finally, in section V, some conclusion will be extracted.

II. POTENTIAL ENERGY SURFACES

An overall picture of the electronic states of reactants and products of this system is displayed in Fig. 1. In the reactant region, the $N(^4S) + H_2^+(X^2\Sigma_g^+)$ channel is located about 1 eV

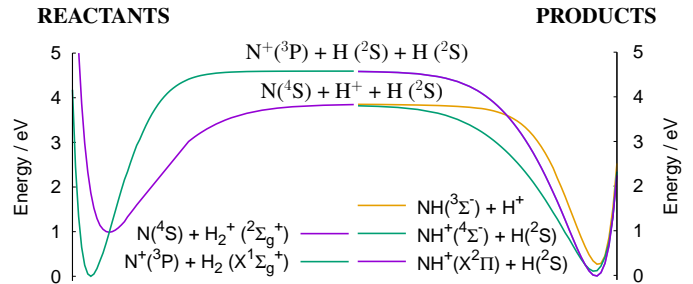


FIG. 1: Asymptotic electronic states for reactants and products

above the $N^+(^3P_{J_A}) + H_2(X^1\Sigma_g^+)$ one so, the former channel will not be populated at the energy range used in this work. Regarding the product region, the lowest channels are $NH^+(X^2\Pi, ^4\Sigma^-) + H(^2S)$ and $NH(^3\Sigma^-) + H^+$ ones.

A. Ab initio calculations for the reactant channel

The $N^+(^3P_g) + H_2(X^1\Sigma_g^+)$ reactant channel has been calculated using a state-average complete active space self-consistent field/multireference configuration interaction (SA-CASSCF/MRCI) method with a VTZ-F12 explicitly correlated atomic basis set as implemented in the MOLPRO program[27]. Without taking spin-orbit coupling into account, three adiabatic electronic states, $^3\Pi$ and $^3\Sigma^-$, correlate with the reactants in the $C_{\infty v}$ group of symmetry. The calculations have been done in the C_s point group of symmetry so that the state average multiconfigurational wave function has included two $^3A''$ and one $^3A'$ states, with the molecule lying on the y - z plane. Subsequent MRCI energies have been obtained at the geometries described in the Supplementary Information (SI). The *ab initio* points have been interpolated using a 3D cubic spline method. Finally, the long-range terms, charge-induced dipole and quadrupole [28–30], have been included for $R > 15 a_0$, using the following switching function of R centered at $20 a_0$:

$$f(R) = \frac{1 - \tanh(0.5 [R - 20.0])}{2} \quad (2)$$

The long-range terms included are described in detail in the Supplementary Information (SI), together with some figures describing the main features of the PESs.

Here we shall use a non-relativistic atomic basis set (hereafter called diabatic basis set) $|L\Lambda S\rangle$, where L and S are the modula of the electronic orbital and spin angular momenta of N^+ , and Λ and Σ their projections, respectively, on the Jacobi body-fixed z -axis. In this basis, the non-relativistic electronic matrix takes the form [31]

$$H = \begin{pmatrix} E_{-1} & V & 0 \\ V & E_0 & V \\ 0 & V & E_1 \end{pmatrix} \quad \text{with} \quad E_{-1} = E_1 \quad (3)$$

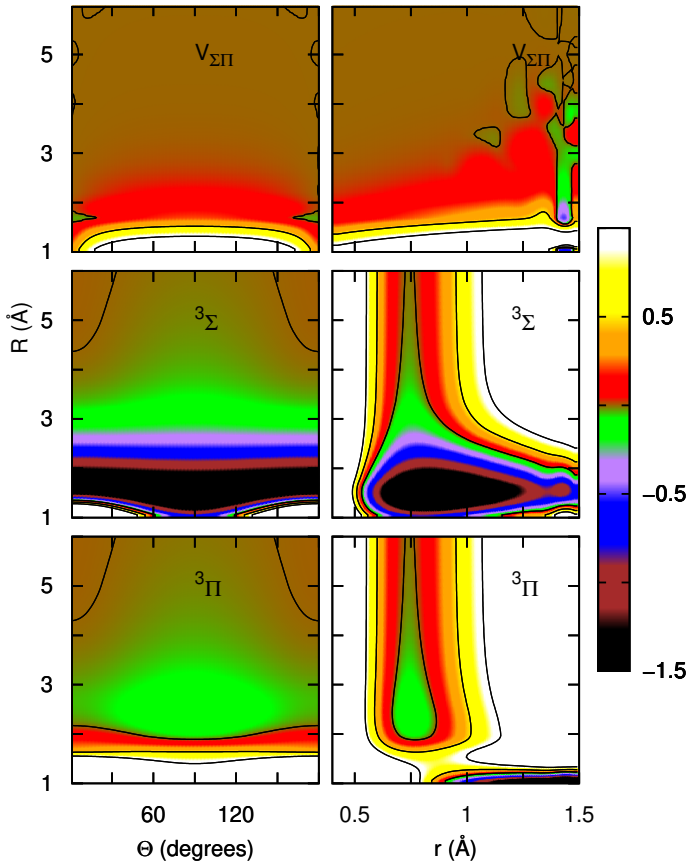


FIG. 2: Contour plots of the PESs for the diabatic ${}^3\Sigma^-$, ${}^3\Pi$ electronic states, and the $\Sigma-\Pi$ coupling, obtained at the H_2 equilibrium distance, $r=0.7 \text{ \AA}$ as a function of the Jacobi distance, R , and the angle γ (left panels) and at $\gamma=90^\circ$ as a function of R and r Jacobi distances. Energies are in eV, and the contour lines are at 0, 0.5 and 1 eV.

whose eigenvalues correspond to the $1^3A''$, $1^3A'$ and $2^3A''$ adiabatic electronic energies. The three unknown E_1 , E_0 and V in Eq. (3) can then be expressed in terms of the *ab initio* energies as [31]

$$\begin{aligned} E_1 &= E_{1^3A'} \\ E_0 &= E_{1^3A''} + E_{2^3A''} - E_{1^3A'} \\ V &= \sqrt{\frac{(E_{1^3A''} - E_{2^3A''})^2 - (E_1 - E_0)^2}{8}}. \end{aligned} \quad (4)$$

These diabatic energies are represented in Fig. 2, and the coupling V in top panels reveal that the coupling between the Σ and Π states become larger in the repulsive parts or the adiabatic PESs, where the $1^3A'$ and $2^3A''$ differ the most.

The spin-orbit basis set, $|J_A \Omega_A\rangle$, is expressed in terms of the diabatic representation $|L \Lambda S \Sigma\rangle$ defined above as

$$|J_A \Omega_A\rangle = \sum_{\Lambda, \Sigma} (-1)^{L-S+\Omega_A} \sqrt{2J_A+1} \begin{pmatrix} L & S & J_A \\ \Lambda & \Sigma & -\Omega_A \end{pmatrix} |L \Lambda S \Sigma\rangle, \quad (5)$$

where $\begin{pmatrix} \dots \end{pmatrix}$ are 3-j symbols. Since H_2 is closed-shell, the

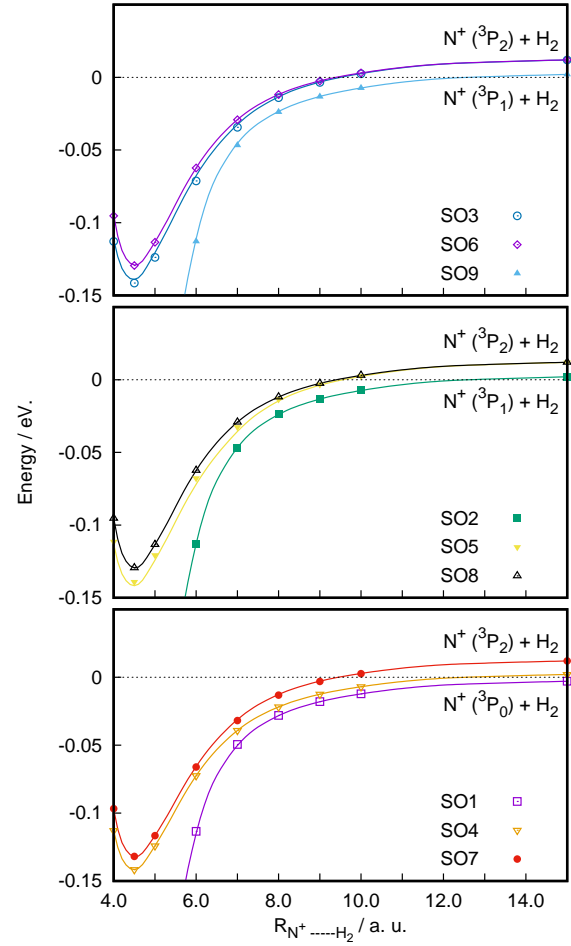


FIG. 3: Energy profiles for the 9 spin-orbit electronic states correlating with $\text{N}^+({}^3P_{J_A=2,1,0})+\text{H}_2$ as a function of the R Jacobi coordinate for $r=1.4 \text{ a.u.}$ and $\gamma=90^\circ$. The energy curves are distributed in three panels (1, 4 and 7 in the bottom panel, 2, 5 and 8 in the middle panel and 3, 6 and 9 in the top panel) to show more clearly the differences between *ab initio* (points) and the diabatic+atomic spin-orbit model (lines), using the *ab initio* spin-orbit splittings.

total orbital (\mathbf{L}) and spin (\mathbf{S}) electronic angular momenta correspond to atom $\text{N}^+({}^3P_{J_A})$, with $\mathbf{J}_A = \mathbf{L} + \mathbf{S}$, so that we shall consider that H_{SO} does not depend on the distance R , and has eigenvectors $|J_A \Omega_A\rangle$, whose E_{J_A} eigenvalues are $(2J_A+1)$ degenerate. Following the treatment of Jouvét and Beswick [19], summarized in the Supplementary Information for completeness, the electronic Hamiltonian is expressed as $H = H_{SO} + H_{el}$, with

$$H_{el} = H_{el}^0 + H_{el}^1 \quad \text{with} \quad \lim_{R \rightarrow \infty} H_{el}^1 = 0, \quad (6)$$

i.e., H_{el}^1 describes the non-relativistic interaction between H_2 and N^+ , while H_{el}^0 describes the two fragment at infinity. The

matrix elements of H_{el}^1 are defined as (see SI and Ref [19])

$$\begin{aligned} \langle J_A \Omega_A | H_{el}^1 | J'_A \Omega'_A \rangle &= \sum_{\Lambda, \Lambda'} \sum_{\Sigma} \sum_k (-1)^{\Omega_A - \Omega'_A} \quad (7) \\ &\times V_{\Lambda \Lambda'}^K(r, R) Y_{K \Lambda' - \Lambda}(\gamma, 0) \sqrt{(2J_A + 1)(2J'_A + 1)} \\ &\times \begin{pmatrix} L & S & J_A \\ \Lambda & \Sigma & -\Omega_A \end{pmatrix} \begin{pmatrix} L & S & J'_A \\ \Lambda' & \Sigma & -\Omega'_A \end{pmatrix}, \end{aligned}$$

In the $|J_A \Omega_A\rangle$ basis set, the atomic spin-orbit Hamiltonian, H_{SO} , is diagonal. The experimental atomic spin-orbit splittings are 48.7 and 130.8 cm^{-1} from NIST[32].

The 9 spin-orbit electronic states correlating with $\text{N}^+(^3P_{J_A=0,1,2}) + \text{H}_2$ have been calculated at MRCI level using the Breit-Pauli operator. At very long distances between N^+ and H_2 , the *ab initio* calculations yield 40.2 cm^{-1} and 120.6 cm^{-1} for the energy of the $\text{N}^+(^3P_1)$ and $\text{N}^+(^3P_2)$ spin-orbit levels, respectively, respect to the energy of the ground spin-orbit state $\text{N}^+(^3P_0)$. These results are in good agreement with the experimental values.

In Fig. 3, the adiabatic spin-orbit energies obtained in the *ab initio* calculations are compared to those obtained diagonalizing the $H_{el} + H_{SO}$ Hamiltonian (see SI for more information), in which the spin-orbit term is considered to only affect $\text{N}^+(^3P_{J_A})$ subsystem, using the *ab initio* spin-orbit splittings. The agreement is fairly good specially at long distances, and only some discrepancies are found in the region of the bottom of the well. This validates the approximation of considering the spin-orbit term only for the N^+ atom in the entrance channel. Within this approximation, electronic transitions between all the spin-orbit states in the entrance channel will be considered in the statistical calculations presented below, using the experimental splittings.

B. *Ab initio* calculations for the product channels

Looking at the products side in Fig. 1, the three lowest channels that could be energetically accessible at the collision energies used in this work correlate with $\text{NH}^+(X^2\Pi) + \text{H}(^2S)$, $\text{NH}^+(a^4\Sigma^-) + \text{H}(^2S)$ and $\text{NH}(^3\Sigma^-) + \text{H}^+$ asymptotes. The $\text{NH}^+(A^2\Sigma^-) + \text{H}(^2S)$ and $\text{NH}^+(b^4\Pi) + \text{H}(^2S)$ channels are too high in energy.

As done for reactants, a SA-CASSCF/MRCI method has been used to calculate the product channels. The electronic states correlating with the three lowest channels without taking into account spin-orbit coupling (in $C_{\infty v}$ point group of symmetry) are shown in Table I.

Since the *ab initio* calculations are done in the C_s symmetry, the state average CASSCF wavefunction has included one $^3A'$, three $^3A''$, one $^1A'$, one $^1A''$ and one $^5A''$ states.

In the products channel, we shall use the adiabatic spin-orbit *ab initio* states, without considering the couplings among them, in contrast with the treatment described above for the reactants channel. We have focused on the states correlating with the two lowest channels, i.e., $\text{NH}^+(X^2\Pi) + \text{H}(^2S)$ and $\text{NH}^+(a^4\Sigma^-) + \text{H}(^2S)$ (see Table I). That involves a total of

Product asymptote	$C_{\infty v}$
$\text{NH}^+(X^2\Pi) + \text{H}(^2S)$	$^3\Pi, ^1\Pi$
$\text{NH}^+(a^4\Sigma^-) + \text{H}(^2S)$	$^5\Sigma^-, ^3\Sigma^-$
$\text{NH}(X^3\Sigma^-) + \text{H}^+$	$^3\Sigma^-$

TABLE I: *Electronic states correlating with the three lowest product channels.*

16 SO states. However, since we need to know the symmetry of the spin-orbit states under the reflection respect to the molecular plane, A' or A'' , the quintuplet electronic states have not been included because they are repulsive and the symmetry treatment is not yet implemented in the Molpro 2015 program. In any case, we have checked that their omission does not affect much the accuracy of the calculations. So, finally, 11 adiabatic spin-orbit energies have been obtained, which are shown in Figs. 4 (see also SI). Among those 11 states, 8 of them correlate with the lowest product channel, $\text{NH}^+(X^2\Pi_{3/2,1/2}) + \text{H}(^2S)$, and the other 3 connect with the $\text{NH}^+(a^4\Sigma^-) + \text{H}(^2S)$ asymptote. Fig 4 shows the energy profiles of the 11 SO-states as a function of the R product Jacobi coordinate, for even and odd symmetries with respect to reflection through the plane of the molecule. These curves show several crossings among the spin-orbit states, which do not occur for all the angles. The anisotropy of the potential depend a lot on the existence or not of such crossings. Thus, the lowest spin orbit states on each symmetry are clearly connected to the deep insertion well for $\gamma > 60^\circ$. However, those intermediates presenting a crossing about $\gamma = 90^\circ$, present a narrower well only in the $60 < \gamma < 120^\circ$, and this will reduce the capture probabilities, as discussed below. Finally, the higher states do not present wells and they will be neglected in the statistical calculations presented in this work.

Another issue which is not yet clear for this system, it is the ergicity of this reaction. Experimentally this reaction has been found to be endoergic by 18 ± 2 meV [6]. Gerlich[33] compared the measured temperature dependencies on the rate constants with a statistical theory for n- H_2 and proposed an endoergicity of 17 meV. Our calculations yield an endoergicity of 80 meV, including zero point energies of reactants and products. Below, we shall use the value of 17 meV.

III. QUANTUM STATISTICAL CALCULATIONS

The thermal reaction rate constant is defined as

$$K(T) = \sum_{q, \beta=1} w_{q, \beta=1}(T) \sum_{q' \beta'} K_{\beta q, \beta' q'}(T) \quad (8)$$

$$\text{with } w_{q, \beta} = \frac{(2I_{bc} + 1)(2j_{bc} + 1)(2J_A + 1)e^{-E_{\beta q}/k_B T}}{\sum_{q'' \beta''} (2I_{bc} + 1)(2j_{bc} + 1)(2J_A + 1)e^{-E_{\beta'' q''}/k_B T}}$$

where the sum is over all vibrational, rotational and electronic states of the reactants, $\text{H}_2(X^1\Sigma^+, v, j) + \text{N}^+(^3P_{J_A})$, of energy $E_{\beta q}$. In these expressions, β, q, m are collective quantum numbers specifying the particular state of reactants and products.

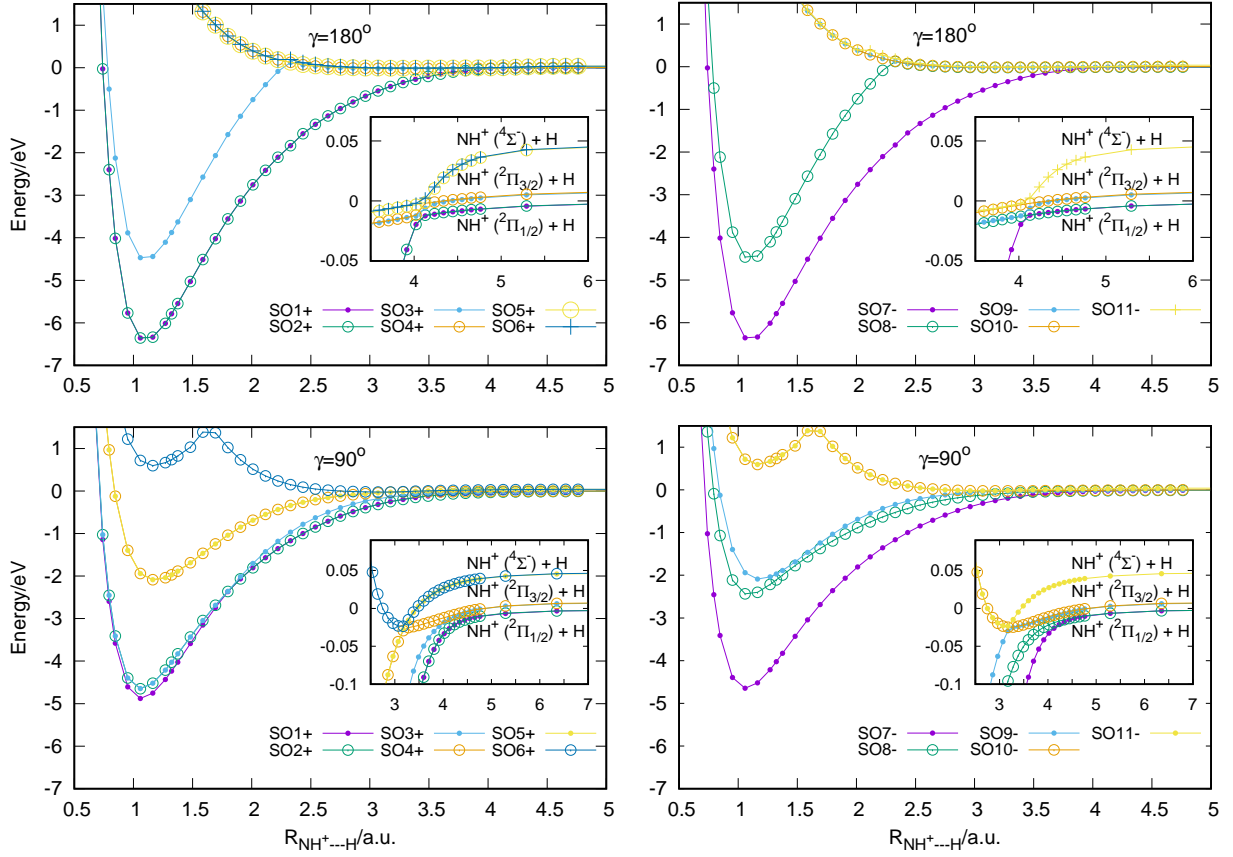


FIG. 4: Energy profiles for the 11 spin-orbit electronic states (6 even, left panels, and 5 odd, right panels, with respect to the reflection through the plane of the molecules) correlating with $\text{NH}^+(\text{X}^2\Pi, \text{a}^4\Sigma^-) + \text{H}(\text{S})$ products as a function of the R Jacobi coordinate for $r = 2$ a.u. and $\gamma = 90$ (bottom panels) and 180 (top panels) degrees. Energies are in eV.

$\beta = 1, 2, 3$ denote the arrangement channel, $\text{H}_2 + \text{N}^+$, and the two equivalent $\text{H} + \text{HN}^+$ and $\text{NH}^+ + \text{H}$ channels of products, respectively. $q = e_{bc}, v_{bc}, j_{bc}, I_{bc}, J_A$ are the electronic, vibrational, rotational and nuclear spin quantum numbers of the BC fragment ($I_{bc} = 0$ and 1 for para/ortho H_2), while J_A denotes the electronic angular momentum of the atomic fragment. Finally, $m = \Omega_{bc}, \Omega_A$ are the projections of the angular momentum of the diatomic and atomic fragment in the body-fixed z -axis, respectively, in each rearrangement channel. $K_{\beta=1q, \beta'q'}(T)$ are the state-to-state rate constants, which correspond to the Boltzmann average over the translation energy, E , of the reaction state-to-state cross section

$$K_{\beta q, \beta' q'}(T) = \sqrt{\frac{8}{\pi \mu (k_B T)^3}} \int dE E \sigma_{\beta q, \beta' q'}(E) e^{-E/k_B T}. \quad (9)$$

The cross section is obtained under the partial wave summation over the total angular momentum, J , and parity under inversion of spatial coordinates, p , as

$$\sigma_{\beta q, \beta' q'}(E) = \frac{\pi}{(2j_{bc} + 1)(2J_A + 1)k_{\beta q}^2(E)} \times \sum_{Jp} \sum_{mm'} (2J + 1) P_{\beta q m, \beta' q' m'}^{Jp}(E), \quad (10)$$

where $k_{\beta q} = \sqrt{2\mu(E - E_{\beta q})}/\hbar$ (with μ being the $\text{H}_2 + \text{N}^+$ reduced mass), and E being the total energy.

$P_{\beta q m, \beta' q' m'}^{Jp}(E) = |S_{\beta q m, \beta' q' m'}^{Jp}|^2(E)$ are the state-to-state reaction probability from a particular initial state (β, q, m) of the reactants to a final state of products (β', q', m'). This quantity can be calculated with different methods, exact and approximate, quantum and classical. In the statistical approach [34, 35] the state-to-state reaction probability is calculated as

$$P_{\beta q m, \beta' q' m'}^{Jp}(E) = C_{\beta q m}^{Jp}(E) B_{\beta' q' m'}^{Jp}(E) \quad (11)$$

with the branching ratio matrix, $B_{\beta' q' m'}^{Jp}$, being defined as

$$B_{\beta' q' m'}^{Jp}(E) = \frac{C_{\beta' q' m'}^{Jp}(E)}{\sum_{\beta'' q'' m''} C_{\beta'' q'' m''}^{Jp}(E)} \quad (12)$$

where the sum in the denominator runs over all the accessible states of reactants and products. For $J = j = 0$ there are many forbidden channels. This factorization, allows to define

a capture cross section as

$$\sigma_{q,\beta=1}^C = \frac{\pi k_{vjA}^{-2}(E)}{(2j+1)(2J_A+1)} \sum_{Jp} \sum_m (2J+1) C_{\beta qm}^{Jp}(E). \quad (13)$$

In the case of very exothermic reactions, the capture cross section coincides with the reactive cross section. In this factorization, we could define approximately the cross section as

$$\sigma_{\beta q,\beta'q'}(E) \approx \sigma_{\beta q}^C(E) \times \mathcal{B}_{\beta'q'}(E) \quad (14)$$

with

$$\mathcal{B}_{\beta'q'}(E) = \sum_{m'} \sum_{Jp} B_{\beta'q'm'}^{Jp}(E), \quad (15)$$

which would only be accurate when the individual $B_{\beta'q'm'}^{Jp}(E)$ do not strongly depend on J and p . Otherwise it can only be taken as an approximation for complex forming reactions.

The different statistical approaches depend on the procedure followed to calculate the $C_{\beta qm}^{Jp}$ capture probabilities. In the present work we use the quantum statistical [21–24], and the adiabatic statistical [20, 36, 37] approaches.

In the quantum statistical approximation, a set of inelastic close-coupled equations is solved for each rearrangement channel independently imposing complex boundary conditions at short distances as described in the Appendix A. For doing so, we have developed here a new program based in the Renormalized Numerov method (called aZticc), as described in the Appendix. The original coupled nuclear-electronic diabatic basis set used for $N^+(^3P_{J_A}) + H_2(v=0, j=0)$ reactants is that of Ref.[19], $|JM\Omega j J_A \Omega_A p\rangle$, which are linear combinations of functions

$$|JM\Omega j J_A \Omega_A\rangle = \sqrt{\frac{2J+1}{8\pi^2}} D_{M\Omega}^{J*}(\phi, \theta, \chi) Y_{j\Omega-\Omega_A}(\gamma, 0) |J_A \Omega_A\rangle, \quad (16)$$

with parity $p = \pm 1$ with respect to inversion of spatial coordinates. The treatment is described in the SI for completeness, where the matrix elements of the different terms of the Hamiltonian are also shown. For products, described in an adiabatic spin-orbit approximation, no correlation among electronic and nuclear angular momenta is considered, and we treat them as a particular case with $L = S = 0$.

The adiabatic statistical approach [20, 36, 37] uses a classical approach for the capture probability, *i.e.*

$$C_{\beta qm}^{Jp} = \begin{cases} 1 & \text{when } E > E_b \\ 0 & \text{when } E < E_b \end{cases}, \quad (17)$$

where E_b is the energy at the top of the barrier associated to the corresponding adiabatic eigenvalue of the matrix $\bar{V}(R)$ appearing in the close-coupling equations, in Eq. (A2).

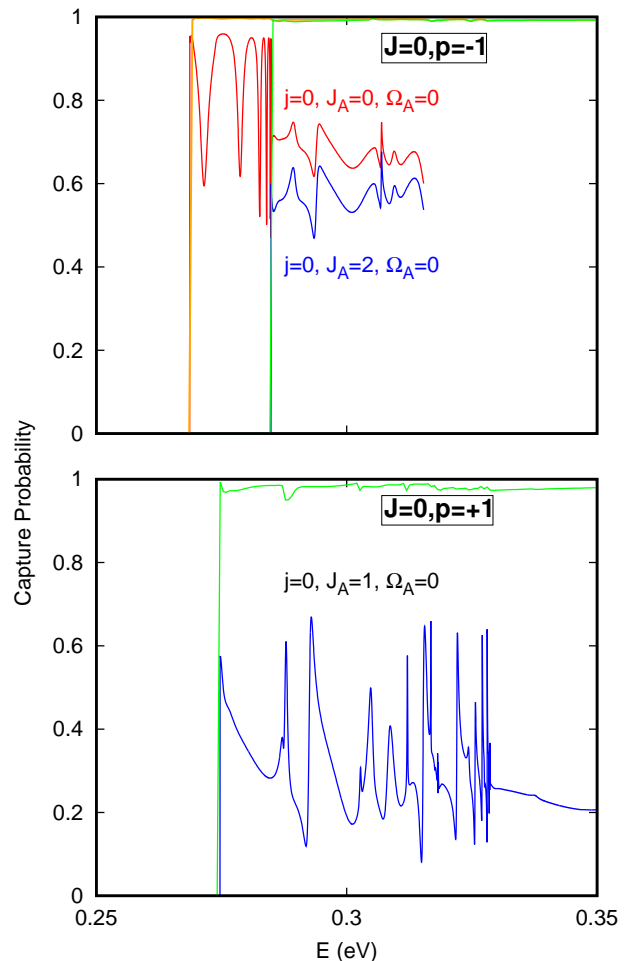


FIG. 5: Quantum capture probabilities obtained for the $N^+(^3P_{J_A}, J_A = 0, 1, 2) + H_2(v=0, j=0)$ for $J = 0$, and $p = +1$, bottom panel, and $p = -1$, top panel. Blue and red probabilities correspond to $R_c = 3$ bohr, while green and orange to $R_c = 4$ bohr

IV. RESULTS AND DISCUSSIONS

A. Quantum versus classical capture probabilities

We start by showing the quantum capture probabilities calculated with the aZticc program, described in the appendix. The details of the numerical calculations are described in the Supplementary Information. In Fig. 5 the capture probabilities obtained for $j=0$, $J=0$ and $p = \pm 1$ are shown, where the full spin-orbit fine structure of $N^+(^3P_{J_A})$ is considered with the symmetry restrictions introduced by the treatment of Jouvet and Beswick[19] (in the SI). The diabatic channel $J_A = 0, \Omega_A = 0$ and $J_A = 2, \Omega_A = 0$ (appearing for $p = -1$) are directly connected to the insertion well and they show a larger capture probability. The diabatic channel $J_A = 1, \Omega_A = 0$ presents a barrier, but it presents a non-negligible capture probability, and this is only possible to non-adiabatic transition.

It is important to note that the quantum capture probabilities

are rather different from the classical ones, which are 1 above the barrier. These results are obtained with a capture radius of $R_c = 3$ and 4 bohr, as indicated in the caption of Fig. 5. The captures probabilities depend on the R_c [24, 38]. To consider other R_c , we can not do it by simply setting $R_{min} = R_c$, because the repulsive electronic states are still open for some energies. Instead, we set the adiabatic-to-adiabatic transfer matrix $\bar{S}_{ij} = 1$ below R_c , in Eq. (A16). By setting $R_c = 4$ bohr, the quantum capture probabilities increase a lot, becoming very close to 1, *i.e.* very similar to the classical capture probabilities using in the adiabatic statistical approach. This demonstrate that capture probabilities decreases because of the transition among different channels, which reflect back part of the incoming flux. The quantum capture converges rapidly, and for $R_c = 3.5$ bohr the results are nearly indistinguishable to those shown for $R_c = 3$ bohr in Fig. 5.

It is important to note here that, depending on the parity, p , and total angular momentum, J , not all the spin orbit-states of the atom, J_A, Ω_A , exist due to symmetry restrictions. This is particularly important for $j=0$, for which only $\Omega = \Omega_A = 0$ exists. For $J = 0, p = +1, j=0$, in the top panel of Fig. 5, only the functions with $J_A = 0, \Omega_A = 0$ and $J_A = 2, \Omega_A = 0$ exist, while for $J = 0, p = -1, j=0$, only $J_A = 1, \Omega_A = 0$ appears. As J and j increases, and therefore Ω , more J_A, Ω_A states participate. This makes appear contributions from the three values of the $J_A = 0, 1$, and 2 to the reactive cross section. This occurs in the quantum as well as in the pure adiabatic statistical approaches, as a consequence of using a coupled basis set for electronic and nuclear angular momenta. This is not the case of previous treatments [17, 18], where it is assumed that only the three lower adiabatic spin-orbit states of $N^+(^3P_{J_A})$, correlating to $J_A = 0$ and 1 react, while the six higher adiabatic spin-orbit states do not react.

In the products channel describing the $NH^+(^2S+1\Lambda_\Omega) + H$ collision, independent adiabatic spin-orbit states are considered in this work. The capture probabilities calculated with the quantum and adiabatic (or classical) approaches are presented in Fig. 6. In general the capture probabilities for a single adiabatic state are larger and with less structure. Narrow resonances are in general absent. For states 3 and 8, the quantum capture is nearly 1 and constant, as in the adiabatic case. This is an indication that the PES anisotropy and anharmonicity do not change from NH^+ products along the channel up to capture. For states 1 and 2, the quantum probability oscillates slightly around 0.95, *i.e.* is rather constant, and the error of the adiabatic capture is of the order of 5%. The most extreme cases are states 4 and 9, for which the quantum capture probability is in the interval 0.7-0.75, so that we consider that in these cases the adiabatic capture produces a relatively large error, of $\approx 30\%$, but nearly constant with energy. This trends persist for higher J , and one possible approximation could be to multiply the adiabatic capture probability by a correction factor, depending on the electronic state and energy independent, and this is done below for the mixed quantum-adiabatic statistical approach.

All these results demonstrate that quantum capture probabilities are in general lower than the classical ones, which take a value of 1 for all the adiabatic electronic states. This reduc-

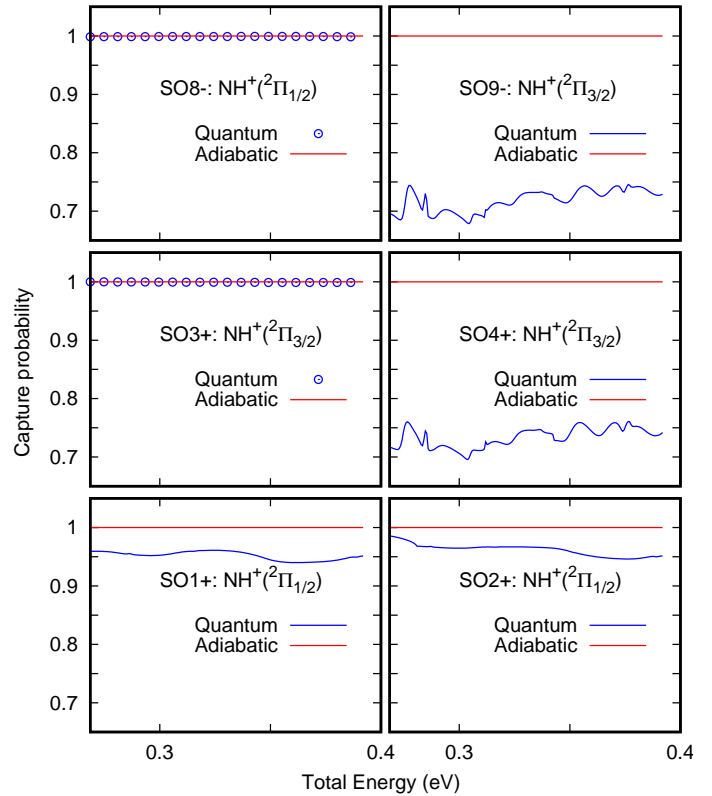


FIG. 6: Capture probabilities obtained for the $NH^+(e, v = 0, j = 0) + H$ for $J = 0$, and $p = +1$, with $R_c = 3$ bohr. Those corresponding to $SO7^-$ is equal to $SO2^+$, $SO5^+$ is $SO4^+$, and $SO6^+$, $SO10^-$ and $SO11^-$ are repulsive with no capture.

tion is particularly important when several electronic states are considered, for which electronic transitions occur specially at the crossings. When only one electronic state is considered, as it is the case for product arrangement, the curves associated to different channels are nearly parallel, what reduces considerably the transitions among them before being captured. In these cases, the quantum capture probabilities are much closer to one, in general, close to the adiabatic statistical approximation. It should be noted, that the anisotropy of the single adiabatic potential (see $SO4^+$ and $SO9^-$ in Fig. 6) introduces crossings among rotational channels that can also reduce the capture.

B. Total reactive cross section

The reaction cross section for this reaction was measured by Sunderlin and Armentrout [7] in a rather broad collision

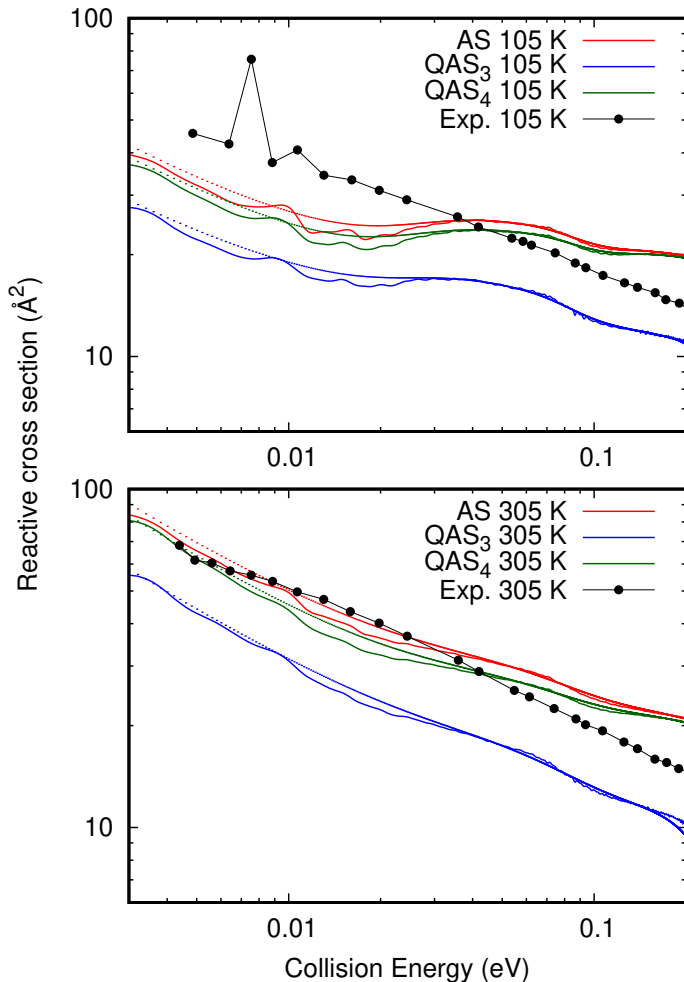


FIG. 7: Thermal Reactive cross section for $H_2+N^+(^3P_{J_A})$, including the thermalized at 305 K (bottom panel) and 105 K (top panel), obtained with the Adiabatic Statistical (AS) and mixed-Quantum/adiabatic statistical (QAS) methods. The experimental values are from Ref. [7]. The results obtained with the two approaches are also convoluted with the Doppler broadening, according to Chantry[39] shown with dotted lines.

energy interval. In these experiments, the H_2 reactants are considered at two temperatures 105 and 305 K, and the results are broadened by the ion energy spread and Doppler broadening [7]. In Fig. 7, the experimental results at 305 K and 105 K are compared with those obtained in this work with the AS and the QAS methods. The theoretical results convoluted with a gaussian accounting for the Doppler broadening according with the method of Chantry[39] are also shown in the figure, showing a slight increase of the cross section. However, this increase is not enough to match the experimental results.

The QAS results, with $R_c = 3$ and 4 bohr (QAS₃ and QAS₄, respectively), are always below the AS results, because the quantum capture probabilities are lower than one, as described

above. At collision energies below 0.03 eV, the AS results at 305K match very well with the experimental results[7]. This is not the case for 105K. Above 0.03 eV, however, the AS and QAS₄ results are above the experimental results, while the QAS₃ are below. In fact, AS/QAS₃ cross section difference increases with energy, because quantum captures continue decreasing, while adiabatic captures are always one above the barrier. Above 0.03 eV (for both temperatures), the experimental results are in between the AS and QAS₃ results, being the QAS₄ probably the best matching the experimental results. At 0.2 eV and below, the main contributions arise from SO1+, SO2+ and SO7-, while the other contributions are minor. The contribution of the more excited states is relatively small at these energies, and even if only the SO1+, SO2+ and SO7- are included, the cross section at 0.2 eV obtained with the AS and QAS₄ methods are always slightly larger than the experimental measurements. However, the QAS₃ is below in all the energy interval considered here.

The AS treatment considers that all the flux overpassing the effective barrier is trapped, and therefore is treated statistically. However, when considering a quantum capture approach, we have demonstrated that it strongly depends on the capture radius [24, 38]. The problem is therefore to determine the trapping region, without introducing artificial bias among different channels. In fact, considering too short capture radius includes inelastic transitions in the so-called trapping region, but only within the same rearrangement channel, while in the pure statistical spirit it should be considered among all rearrangement channels. To avoid this bias, here we used the AS results as a benchmark to determine the best capture radius, without including any unbalance among the different rearrangement channels, what leads to the optimal value of $R_c=4$ bohr in this case, close to the average position of the effective barrier used in the AS method.

It is worth mentioning, that AS and QAS₄ results above 0.2 eV also overestimate the reaction cross section. The reason for this is attributed to the large mass mismatch between N^+ and H_2 subsystems, which reduces the energy transfer probability. Statistical assumption, however, implies that energy is completely redistributed among all degrees of freedom, yielding to an overestimation of the reaction cross section. This is demonstrated in the SI, where statistical results are compared with complete quantum calculations performed with the wave packet code MADWAVE3[40, 41] using the single adiabatic potential energy surface, PES IV of Ref. [14].

The simulated cross sections change a lot varying the temperature from 105 to 305 K. The temperature mainly affects the rotational distribution of H_2 in the cell. The cross sections for the individual initial states of the reactants show that $H_2(j=0)$ is closed for $J_A = 0$ and 1 below 0.01 eV, while it is open for all J_A and for $H_2(j=1)$ at all collision energies. This clearly explains why theoretical thermal cross section varies so much from 105 to 305 K. These changes, however, are not so important in the experimental results, which show a good agreement at 305 K with the AS and QAS₄ results, while the agreement is much worse at 105 K.

In order to improve the experimental/theoretical agreement, different exothermicities have been considered. This was also

done by Grozdanov and McCarroll[17], who increased the endothermicity from 18.45 meV to 23.45 meV to reduce their cross section, which was slightly overestimated in their approach as compared to the experimental thermal cross section. However, the variation of the endothermicity, in all cases considered in this work, yield rate constants in considerably worse agreement with the available experimental measurements, performed in several studies with different techniques. We therefore conclude that the cross sections measured by Sunderlin and Armentrout [7] at 105 K are also affected by the ion energy spread, as discussed by these authors, which is not accounted for in this work because the exact conditions of those experiments are not known. We also conclude that the endothermicity of 17 meV is the best choice, as shown below.

C. Rate constants

The thermal rate constants for ortho- H_2 fraction $f=0.005$ and 0.75, of H_2 are shown in Fig. 8 and compared with the available experimental data, for the AS (bottom panel), QAS₄ (middle panel) and QAS₃ (top panel) methods. There is a rather good qualitative agreement between the two simulated rate constants (AS and QAS₃ and QAS₄) and the experimental results. The QAS₃ results for $f=0.005$ agree very well with the experimental measurements of Zymak and et al.[8], and for $f=0.75$ lies in between the three sets of experimental results for temperatures below 50 K. However, for $T > 50$ K and $f=0.75$, the QAS₃ results are considerably lower than any set of experimental results. The QAS₄ and AS results are in between all the sets of experimental data in the whole temperature interval considered here, being in general closer to those of Fanghanel[9]. The difference between experimental results allows to establish a certain error, probably due to the exact ortho- H_2 fraction f .

The variation of the rate constants for more values of f are shown in Fig. 9, for the two best theoretical results, QAS₄ (top panel) and AS (bottom panel). For $f = 0$ (para- H_2), the experimental results of Zymak *et al*[8] (which were extrapolated) are in better agreement with the QAS results than with the pure AS. However, for $f = 1$ (ortho- H_2) the agreement at higher temperatures is better for the AS results than for the QAS. This is probably because the AS results are larger at 0.01 eV than the QAS, and in better agreement with the experimental cross sections, in Fig. 7. The overall agreement of the two simulations, AS and QAS, is in general excellent for temperatures between 20 and 100 K, and the increase of the error for $T < 20$ K could be attributed to small contamination of ortho/para ratios, as well as to inaccuracies of the simulations.

The agreement between the two sets of experimental rate constants also show some discrepancies. These discrepancies are similar in magnitude to that between simulations and experiments. It is important to note the large variation of the rate constant as a function of the ortho- H_2 fraction, f , due to the fact that the reaction is exothermic for ortho- $H_2(j=1)$, while it is closed for para- $H_2(j=0)$, whose ratios may change slightly.

Moreover, a similar situation holds for the spin-orbit states

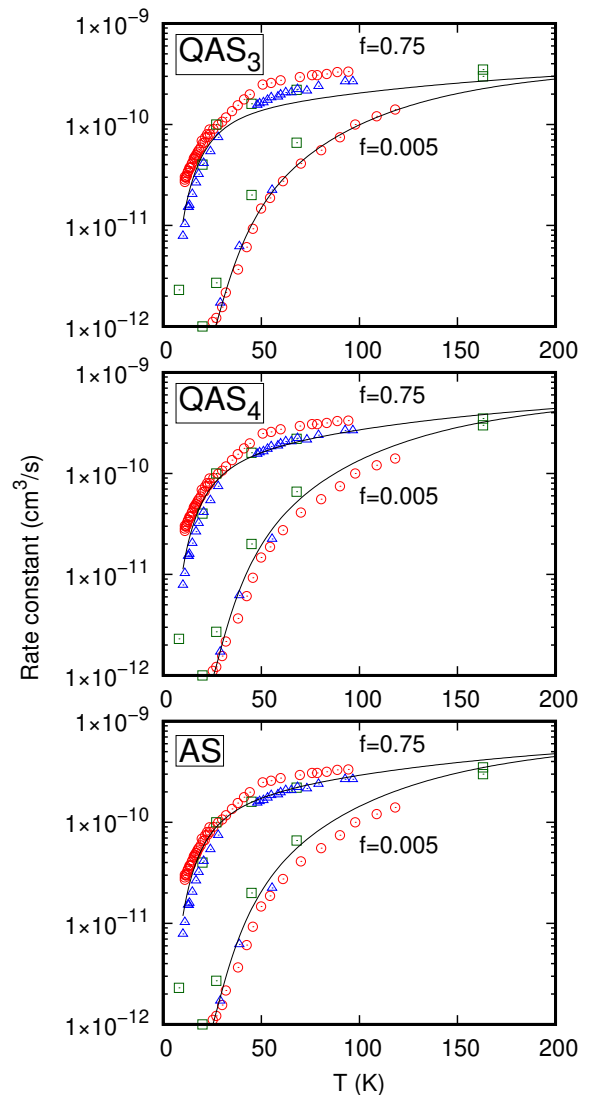


FIG. 8: Thermal Reactive rate constants for $H_2 + N^+(^3P_{J_A})$, obtained for the two limiting experimental o - H_2 fractions, $f=0.005$ and $f=0.75$ (n - H_2), as a function of temperature. Symbols are the experimental results: open circles by Zymak and et al.[8], open square are taken from Table II of Marquette et al.[6] (the value list at 27 K for n - H_2 has been corrected to read $2.7 \cdot 10^{-12}$) and open triangles are the results of Fanghanel[9]. Lines are the simulated rate constants with QAS₃ (top panel), QAS₄ (middle panel) and the AS (bottom panel) described in this work.

of $N^+(^3P_{J_A})$: for $H_2(j=1)$ all $J_A=0$ and 1 states are open, while for $H_2(j=0)$ only $J_A=2$ is open. The individual rate constants for each J_A spin-orbit state and different ortho- H_2 fractions are shown in Fig. 10. In the two formalisms, AS and QAS, the rate constants for the 3 spin-orbit states are non-zero. Such situation may introduce changes in the experimental determinations of the state specific rate constants, as discussed by Zymak *et al.*[8] and Fanghanel[9].

AS and QAS methods yields to rather different rate constants for each individual J_A spin-orbit state. The AS method tends to produce a progression $J_A = 0, 1$ and 2, with the rate

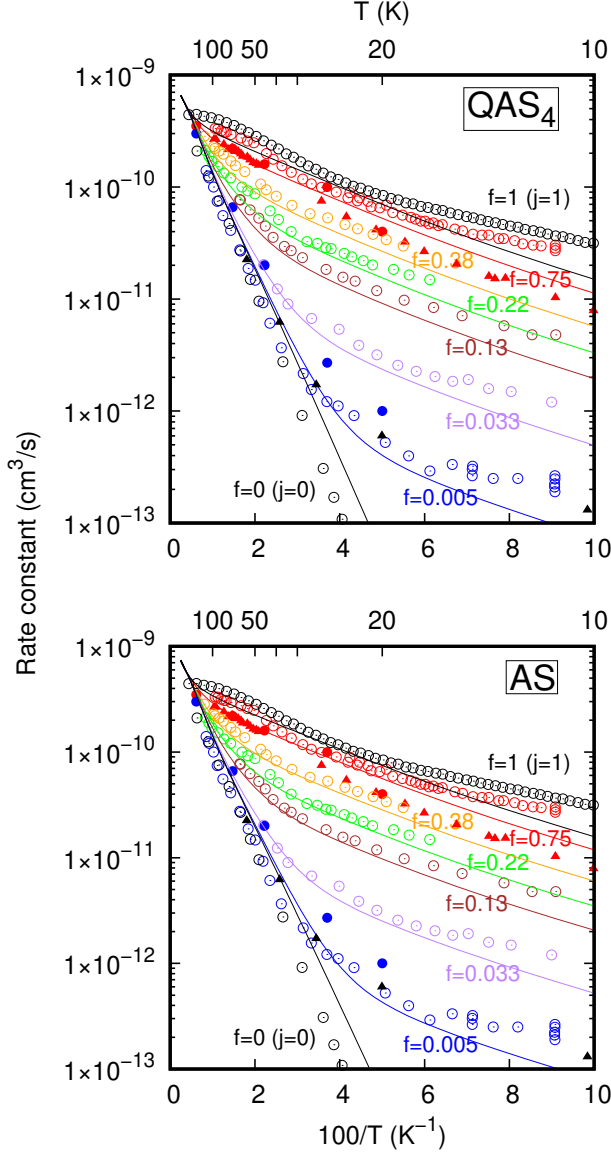


FIG. 9: Thermal Reactive rate constants for $H_2 + N^+(^3P_{J_A})$, obtained for different o - H_2 fractions, as described by Zymak and et al.[8]. Open circles are the experimental results extracted from Fig. 4 by Zymak and et al.[8] (note that for $f=0$ and 1, their values are extrapolated). Full circles are taken from Table II of Marquette et al.[6]. Triangles are the experimental results of Fanghanel[9]. Top panel show the mixed Quantum and Adiabatic statistical results for $R_c = 4$ bohr (QAS_4), bottom panel show the pure Adiabatic Statistical results (AS). In all cases, the population of the J_A spin-orbit states correspond to a Boltzmann distribution.

for $J_A=2$ being the larger, simply because it correspond to the most endothermic case. The situation varies a lot for the QAS results, for which the rates for all J_A are closer and their relative importance varies with temperature. This result is a consequence of the explicit treatment of transitions among spin-orbit states, using correlated electronic-nuclear diabatic

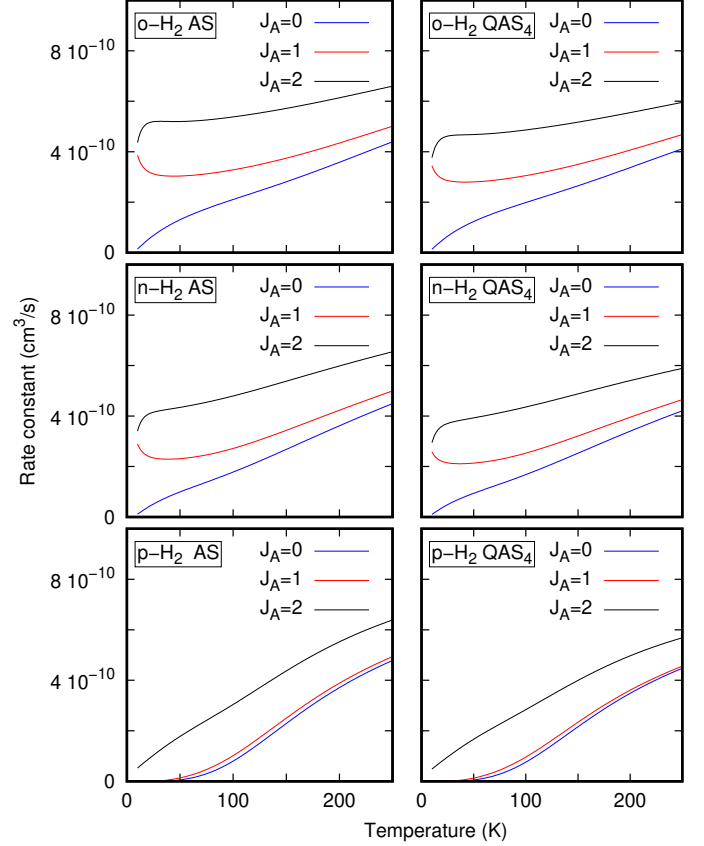


FIG. 10: Thermal Reactive rate constants for $H_2 + N^+(^3P_{J_A})$, for $ortho$, natural and $para$ H_2 for each $N^+(^3P_{J_A})$ spin-orbit state, obtained with the AS (left panels) and QAS_4 (right panels) methods.

basis set. Since this is accounted for more exactly in the QAS method, in contrast to the AS one, we conclude that the QAS J_A -dependent rate constants are more accurate. The numerical values of the J_A -dependent rate constants are given in the SI. Our results are in general in better agreement with the experimental results of Fanghanel[9], where the reactivity of $N^+(^3P_{J_A=2})$ is considered to be non-zero, as it is demonstrated in this work.

The accurate determination of the reaction rate constants is important to improve the accuracy of astrophysical models. The rate constant available in the Kida Data base for this reaction at low temperatures corresponds to the value reported by Marquette et al.[6] for the n - H_2 (corresponding to an ortho-fraction of $f=0.75$). These experimental values are compared with the present results in Figs. 8 and 9. This reaction, however, strongly depends on the initial rotational state of H_2 and also on the spin-orbit state of $N^+(^3P_{J_A})$, as shown in this work. In detailed astronomical models, it is important to incorporate the specific rate, at least for ortho and para hydrogen. For this reason we provide in the Supplementary

Information the parameters obtained in a fit of the numerical rate constants obtained in this work, and shown in Fig. 10, for each ortho-fraction of H₂ and each electronic J_A value for N⁺, listed in a Table.

V. CONCLUSIONS

In this work we have studied the spin-orbit dependence of the rate constants for the N⁺(³P_{*J_A*) + H₂ → H + NH⁺(²Π_{1/2,3/2). The potential energy surfaces on reactants and products channels have been calculated separately, using accurate *ab initio* methods. In the reactants N⁺(³P_{*J_A*) + H₂ channel, the couplings among the spin-orbit states have been calculated, using a diabaticization method together with a model based on atomic spin-orbit localized in the N⁺ cation. This method has been compared with accurate *ab initio* calculations showing excellent agreement. The NH⁺(²Π_{1/2,3/2, ⁴Σ⁻) + H products potential energy surfaces have been calculated in the adiabatic spin-orbit approximation.}}}}

To account explicitly for the spin-orbit couplings, the treatment of Jouvet and Beswick[19] have been implemented within two statistical models: an adiabatic statistical (AS) model and a mixed quantum and adiabatic statistical (QAS) method. A variation of the renormalized Numerov method has been developed to treat open-quantum boundary conditions, needed to calculate quantum capture probabilities, used in the mixed quantum-adiabatic statistical method.

It is worth noting, that the AS model provide quite accurate rates for all spin-orbit states of N⁺(³P_{*J_A*), $J_A=0, 1$ and 2, when the basis is formed by proper symmetry functions combining electronic (spin and orbital) and nuclear angular momenta. On the contrary, when the adiabatic approximation is done at the spin-orbit electronic states alone first, only the first 3 spin orbit states (correlating to $J_A=0$ and 1) can contribute to the reactive cross section and rate constants.}

Thermal cross section and rate constants have been calculated and compared with the available experimental measurements. The calculated thermal rate constants for different ortho fractions of H₂ show reasonable good agreement with the experimental measurements of Marquette *et al.*[6], Zymak *et al.*[8] and Fanghanel[9], confirming an endothermicity of 17 meV. We find that the three J_A spin-orbit states have an appreciable contributions rate constants for all the o-H₂ fractions, f , measured. In particular, the possible effect of $J_A=2$ in the determination of the rate constants for $f=0$ and 1 (not directly measured) was not taken into account by Zymak *et al.*[8] and it was included and discussed by Fanghanel[9]. We demonstrate here, that it is important to be included for this system, since there are many different energy thresholds, for reactants (J_A and j values) and products, and are of particular interest for astro physics models of cold molecular clouds.

VI. SUPPLEMENTARY MATERIAL

See supplementary material for detailed description of the *ab initio* calculations for the reactants and product channels, for the computational details of the dynamical calculations, the treatment used to treat the collisions of open shell atoms with closed shell diatomic molecules, and the state-specific rate constants for the different spin-orbit states of N⁺(³P_{*J_A*) and ortho and para H₂ are described and provided in separate files.}

VII. ACKNOWLEDGEMENTS

We want to thank Prof. P. Armentrout for providing us the experimental values of the cross section measurements. The research leading to these results has received funding from MICIYU under grant No. PID2021-122549NB-C2. The calculations have been performed in Trueno-CSIC and CCC-UAM.

VIII. DATA AVAILABILITY

The data that support the findings of this study are available from the authors upon reasonable request.

Appendix A: Quantum capture method

1. Diabatic representation

The method used here to evaluate the quantum capture probabilities is very similar to that previously described by Rackham *et al.*[21]. Expanding the total wave function in a diabatic basis set as

$$\Psi^\beta(R, \mathbf{x}) = \sum_n \Phi_\alpha^\beta(R) \varphi_\alpha(\mathbf{x}) \quad (\text{A1})$$

The close-coupling equations can be written as

$$\begin{aligned} \frac{\partial^2 \Phi_\alpha^\beta(R)}{\partial R^2} &= \frac{2\mu}{\hbar^2} \sum_{\alpha'} \{V_{\alpha\alpha'}(R) - E\delta_{\alpha\alpha'}\} \Phi_{\alpha'}^\beta(R) \quad (\text{A2}) \\ &\equiv \bar{\Phi}''(R) = \frac{2\mu}{\hbar^2} \{\bar{V}(R) - \bar{1}E\} \bar{\Phi}(R) \end{aligned}$$

where α, β denotes the collections of quantum numbers needed to specify the channels, and $\bar{\Phi}$ is a vector and \bar{V} is a matrix. Eq.(A2) are solved here using a Numerov-Fox-Goodwin or renormalized Numerov method [42, 43], in which each of the quantities is discretized in a radial grid of N equidistant R_i points, with $\Delta = R_{i+1} - R_i$. Denoting $\Phi(R = R_i) = \Phi_i$ and $\bar{V}(R = R_i) = \bar{V}_i$, and doing a Taylor expansion of the coefficients and their second derivatives, a three points Numerov relationship is found

$$\bar{\alpha}_{i-1} \bar{\Phi}_{i-1} + \bar{\beta}_i \bar{\Phi}_i + \bar{\gamma}_{i+1} \bar{\Phi}_{i+1} = 0 \quad (\text{A3})$$

where

$$\begin{aligned}\bar{\alpha}_{i-1} &= \bar{\mathbf{1}} - \frac{\Delta^2}{12} \left\{ \frac{2\mu}{\hbar^2} (\bar{V}_{i-1} - E\bar{\mathbf{1}}) \right\} \\ \bar{\beta}_i &= -2\bar{\mathbf{1}} - \frac{10\Delta^2}{12} \left\{ \frac{2\mu}{\hbar^2} (\bar{V}_i - E\bar{\mathbf{1}}) \right\} \\ \bar{\gamma}_{i+1} &= \bar{\mathbf{1}} - \frac{\Delta^2}{12} \left\{ \frac{2\mu}{\hbar^2} (\bar{V}_{i+1} - E\bar{\mathbf{1}}) \right\},\end{aligned}\quad (\text{A4})$$

with an error proportional to Δ^6 .

The Fox-Goodwin algorithm consists in defining

$$\bar{\Phi}_i = \bar{\mathcal{R}}_i \bar{\Phi}_{i+1} \quad (\text{A5})$$

so that imposing the boundary condition at $i=1$, the $\bar{\mathcal{R}}_i$ is propagated according

$$\bar{\mathcal{R}}_i = - \left\{ \bar{\alpha}_{i-1} \bar{\mathcal{R}}_{i-1} + \bar{\beta}_i \right\}^{-1} \bar{\gamma}_{i+1}$$

until $i=N$, where the second boundary conditions of incoming plus outgoing waves are imposed.

Usually, a real $\bar{\Phi}_i$ is propagated to simplify the calculation because the potential is also real and a regular solution with $\bar{\Phi}_{i=0} = 0$ is imposed because $\bar{V}_1 > E$ for all the channels involved.

On the contrary, in the case of capture in a well, it is assumed that the $\bar{V}_1 < E$ for some of the channels. In order to impose the boundary condition, a transformation to a new adiabatic basis is first done by diagonalizing the potential matrix at $i=1$ as

$$\bar{V}_i \bar{iT} = \bar{D}_i \bar{iT}, \quad (\text{A6})$$

where \bar{D} is a diagonal matrix with the eigenvalues and \bar{T} are the transformation matrix. In this adiabatic representation the coefficients are denoted Ψ to be distinguished from those of the original ‘‘diabatic’’ basis, and the boundary outgoing conditions are applied as

$${}^1\Phi_\alpha(R < R_1) = \begin{cases} 0 & \text{if } D_\alpha > E \\ -i\sqrt{\frac{2\mu}{\pi\hbar^2 k_\alpha}} S_\alpha^T(E) e^{-ik_\alpha R} & \text{if } D_\alpha < E \end{cases} \quad (\text{A7})$$

where it is being assumed that $\bar{V}_i = \bar{V}_1$ for $i < 1$, *i.e.* that the potential is constant at R distances shorter than R_1 , the capture distance. In this expression $k_\alpha = \sqrt{2\mu(E - d_\alpha)}/\hbar$ and $|S_\alpha^T(E)|^2$ is the capture probability, since it correspond to the flux going to $R < R_1$. Under this assumptions in the adiabatic representations we have

$$\bar{\mathcal{A}} = [\bar{i}\Phi_1]^{-1} \quad {}^0\bar{\Phi}_0 = \begin{cases} e^{-|k_\alpha|\Delta} & \text{if } D_\alpha > E \\ e^{-ik_\alpha\Delta} & \text{if } D_\alpha < E \end{cases} \quad (\text{A8})$$

Transforming back to the diabatic representation in which the integration is performed, we get ($i=1$)

$$\bar{\mathcal{R}}_i = \bar{iT}^{-1} \bar{\mathcal{A}} \bar{iT}. \quad (\text{A9})$$

After defining the propagation matrix in the first point of the grid, $\bar{\mathcal{R}}_i$ is iteratively propagated from $i=2$ to N , where the usual incoming/outgoing boundary conditions are imposed as

$$\Phi_\alpha(R_N) = \begin{cases} e^{-|k_\alpha|R} & \text{if } V_{\alpha,\alpha}(R_N) > E \\ i\sqrt{\frac{2\mu}{\pi\hbar^2 k_\alpha}} \left[e^{-i(k_\alpha R - \ell\pi/2)} \delta_{\beta,\alpha} \right. \\ \left. - S_{\alpha\beta}^R(E) e^{i(k_\alpha R - \ell\pi/2)} \right] & \text{if } V_{\alpha,\alpha}(R_N) < E \end{cases} \quad (\text{A10})$$

In the usual procedure, $\bar{\mathcal{R}}_i$ is real and real boundary conditions are imposed to calculate the symmetric reaction matrix, K , and from it the S-matrix which is unitary. In the present case, $\bar{\mathcal{R}}_1$ is complex, all this procedure is done in the complex plane, and assuming that the integration is done until sufficiently long distance, Eq.(A10) is also fulfilled at R_{N-1} , and the S-matrix is directly obtained from the propagation matrix as

$$\begin{aligned}\bar{\mathcal{S}}^R &= [\bar{\mathcal{R}}_{N-1} \bar{\mathcal{P}}_N - \bar{\mathcal{P}}_{N-1}]^{-1} \\ &\times [\bar{\mathcal{M}}_{N-1} - \bar{\mathcal{R}}_{N-1} \bar{\mathcal{M}}_N] \end{aligned} \quad (\text{A11})$$

where \mathcal{M}_i and \mathcal{P}_i are diagonal matrices with elements defined as

$$\begin{aligned}\mathcal{M}_{\alpha\alpha}(R_i) &= \begin{cases} e^{-|k_\alpha|R} & \text{if } V_{\alpha,\alpha}(R_i) > E \\ \sqrt{\frac{2\mu}{\pi\hbar^2 k_\alpha}} e^{-i(k_\alpha R - \ell\pi/2)} & \text{if } V_{\alpha,\alpha}(R_N) < E \end{cases} \\ \mathcal{P}_{\alpha\alpha}(R_i) &= \begin{cases} 0 & \text{if } V_{\alpha,\alpha}(R_i) > E \\ \sqrt{\frac{2\mu}{\pi\hbar^2 k_\alpha}} e^{i(k_\alpha R - \ell\pi/2)} & \text{if } V_{\alpha,\alpha}(R_N) < E \end{cases} \end{aligned} \quad (\text{A12})$$

The resulting $S^R(E)$, in Eq.(A10) is not, in general, unitary. This is evident by inspection of Eq.(A7), since for those channels with $D_\alpha < E$ there is a flux that is trapped at distances $R < R_1$. If all $D_\alpha > E$ the normal situation is got, and the S^R -matrix becomes unitary. The capture probability for a given initial channel is then obtained as

$$C_\beta(E) = |S_{\beta\beta}^T|^2 = 1 - \sum_\alpha |S_{\beta\alpha}^R|^2. \quad (\text{A13})$$

2. Adiabatic-by-sectors representation

The number of channels increases very rapidly with total angular momentum, specially with many electronic states, as considered here. In order to reduce the number of channels we have implemented a variant of the adiabatic-by-sectors method [44–47]. In brief, this method consists in diagonalizing the \bar{V}_i matrix in the close-coupling equations, Eq. (A2) as in Eq. (A6). The new adiabatic functions, iA_p , depend on the collision coordinate R_i , are expressed in the original dia-

batic basis set as

$$\begin{aligned} |iA_p\rangle &= \sum_{\alpha} |\varphi_{\alpha}\rangle^i T_{\alpha p} \equiv \bar{i}A = \bar{\varphi} \quad \bar{i}T \\ |\varphi_{\alpha}\rangle &= \sum_p |iA_p\rangle^i T_{\alpha p} \equiv \bar{i}\varphi = \bar{A} \quad \bar{i}T^{-1}. \end{aligned}$$

The total wave function, Eq. A1, in the new basis set takes the form

$$\Psi^{\beta}(R, \mathbf{x}) = \sum_p |iA_p\rangle^i \Phi_p^{\beta} \rightarrow \bar{i}\Phi = \bar{i}T \quad \bar{\Phi} \quad (\text{A14})$$

The Numerov auxiliary matrices in Eq. (A3) can be re-expressed in the adiabatic representation as

$$\begin{aligned} \bar{i-1}\alpha_{i-1} &= \bar{i-1}T^{-1} \quad \bar{\alpha}_{i-1} \quad \bar{i-1}T = \bar{\mathbf{I}} - \frac{\Delta^2}{12} \left\{ \frac{2\mu}{\hbar^2} (\bar{D}_{i-1} - E\bar{\mathbf{I}}) \right\} \\ \bar{i}\alpha_{i-1} &= \bar{i}T^{-1} \quad \bar{\alpha}_{i-1} \quad \bar{i}T = \bar{S}_{ii-1} \quad \bar{i-1}\alpha_{i-1} \quad \bar{S}_{ii-1}^{-1}, \end{aligned} \quad (\text{A15})$$

and similarly for $\bar{\beta}_i$ and $\bar{\gamma}_{i+1}$ matrices, where the transfer matrix has being defined as

$$\bar{S}_{ij} = \bar{i}T^{-1} \bar{j}T. \quad (\text{A16})$$

Doing some algebra, the recurrence equation of the propa-

gation matrix, Eq. (A6) becomes

$$\bar{i+1}\mathcal{R}_i = - \left\{ \bar{i+1}\alpha_{i-1} \quad \bar{i+1}\mathcal{R}_{i-1} \quad + \quad \bar{i+1}\beta_i \right\}^{-1} \quad \bar{i+1}\gamma_{i+1} \quad (\text{A17})$$

where $\bar{i+1}\mathcal{R}_i$ is the propagation matrix connecting the function i and $i+1$, represented in the adiabatic basis at $i+1$, and

$$\bar{i+1}\mathcal{R}_{i-1} = \bar{S}_{i+1i} \quad \bar{i}\mathcal{R}_{i-1} \quad \bar{S}_{i+1i}^{-1} \quad (\text{A18})$$

with $\bar{i}\mathcal{R}_{i-1}$ being obtained in the previous iteration. Eq. (A17) can be iteratively solved analogously to procedure in the diabatic representation with the extra-effort of transforming the matrices from one point to the following one. In this adiabatic representation, the first value is that $\bar{1}\mathcal{R}_0 = \bar{\mathcal{A}}$, defined in Eq. (A8). Also, the diabatic and adiabatic representation coincide for $i=N$, so that $\bar{N}\mathcal{R}_{N-1} \equiv \bar{\mathcal{R}}_{N-1}$ and the outer boundary conditions are imposed as in Eq. (A10).

The advantage of using the adiabatic-by-sector propagation is that we can reduce the number of channels, by keeping only those which has an energy $E_a(R) < E_{cut}$ for all distances R . This propagator has been implemented in the aZticc program for A + BC collisions, for the case of open shell atom + closed diatom following the work of Jouvet and Beswick [19], described in the Supplementary Information.

-
- [1] V. Wakelam, I. Smith, E. Herbst, J. Troe, W. Geppert, H. Linartz, K. Öberg, E. Roueff, M. Agúndez, P. Pernot, H. M. Cuppen, J. C. Loison, and D. Talbi, “Reaction networks for interstellar chemical modelling: Improvements and challenges,” *Space Science Rev.* **156**, 13 (2010).
- [2] R. Le Gal, P. Hily-Blant, A. Faure, G. Pineau des Forêts, C. Rist, and S. Maret, “Interstellar chemistry of nitrogen hydrides in dark clouds,” *Astron. Astrophys.* (2013).
- [3] A. C. Cheung, D. M. Rank, C. H. Townes, D. D. Thornton, and W. J. Welch, *Phys. Rev. Lett.* **21**, 1701 (1968).
- [4] C. M. Persson, J. H. Black, J. Cernicharo, J. R. Goicoechea, G. E. Hassel, E. Herbst, M. Gerin, M. de Luca, T. A. Bell, A. Coutens, E. Falgarone, P. F. Goldsmith, H. Gupta, M. Kaźmierczak, D. C. Lis, B. Mookerjee, D. A. Neufeld, J. Pearson, T. G. Phillips, J. Sonnentrucker, P. Stutzki, C. Vastel, S. Yu, F. Boulanger, E. Dartois, P. Encrenaz, T. R. Geballe, T. Giesen, B. Godard, C. Gry, P. Hennebelle, P. Hily-Blant, C. Joblin, R. Kolos, J. Křexilowski, J. Martín-Pintado, K. Menten, R. Monje, M. Perault, R. Plume, M. Salez, S. Schlemmer, M. Schmidt, D. Teyssier, I. Péron, P. Cais, P. Gaufre, A. Cros, L. Ravera, P. Morris, S. Lord, and P. Planeas, “Nitrogen hydrides in interstellar gas. herchel/hifi observations towards g10.6-0.4 (w31c),” *Astron. Astrophys.* **521**, L45 (2010).
- [5] P. Hily-Blant, G. Pineau des Forêts, A. Faure, R. Le Gal, and M. Padovani, *Astron. Astrophys.* **557**, A65 (2013).
- [6] J. B. Marquette, C. Rebrion, and B. R. Rowe, *J. Chem. Phys.* **89**, 2041 (1988).
- [7] L. S. Sunderlin and P. B. Armentrout, *J. Chem. Phys.* **100**, 5639 (1994).
- [8] I. Zymak, M. Hejduk, D. Mulin, R. Plasil, J. Glosík, and D. Gerlich, “Low-temperature ion-trap studies of $N^+(\text{}^3P_j) + H_2(j) \rightarrow NH^+ + H$,” *Astrophys. J.* **768**, 86 (2013).
- [9] S. Fanghänel, “Low temperature collisions and reactions in a 22-pole ion trap,” PhD thesis **University of Köln** (2018).
- [10] M. González and A. Aguilar and Y. Fernández, “Analysis of the importance of the 3A_2 NH_2^+ minimum in the ion-molecule reaction $N^+(\text{}^3P)+H_2 \rightarrow NH^++H$ by quasi-classical trajectory method using a plausible single surface model,” *Chem. Phys.* **104**, 57 (1986).
- [11] M. González and A. Aguilar and R. Sayós, “Low energy dynamics, isotopic effects and detailed microscopic reaction dynamics of the ion-molecule reaction $N^+(\text{}^3P)+H_2 \rightarrow NH^++H$,” *Chem. Phys.* , 137 (1989).
- [12] U. Wilhelmsson, P. E. M. Siegbahn, and R. Schinke, “A three-dimensional potential energy surface for the reaction $N^+(\text{}^3P) + H_2(\text{}^1\Sigma_g^+) \rightarrow NH^+(X^2\Pi) + H(2S)$,” *J. Chem. Phys.* **96**, 8202 (1992).
- [13] U. Wilhelmsson and G. Nyman, “A low energy quasiclassical trajectory study of N^++H_2 . Potential energy surface effects,” *J. Chem. Phys.* **96**, 1886 (1992).
- [14] U. Wilhelmsson and G. Nyman, “A low energy quasiclassical trajectory study of N^++H_2 $N^+ + D_2$. Dynamics, cross sections and rate constants,” *J. Chem. Phys.* **96**, 5198 (1992).
- [15] C. L. Russell and D. E. Manolopoulos, “Time-dependent wave packet study of the $N^+ + H_2$ reaction,” *J. Chem. Phys.* **110**, 177 (1999).
- [16] Z. Yang and S. Wang and J. Yuan and M. Chen, “Neural net-

- work potential energy surface and dynamical isotope effects for the $N^+(^3P) + H_2 \rightarrow NH^+ + H$ reaction,” *PCCP* **21**, 22203 (2019).
- [17] T. P. Grozdanov and R. McCarroll, “Statistical Theory of Low-Energy Reactive Collisions of N^+ Ions with H_2 , D_2 , and HD Molecules,” *J. Phys. Chem. A* **119**, 5988 (2015).
- [18] T. P. Grozdanov, R. McCarroll, and E. Roueff, “Reactions of the $N^+(^3P)$ ions with H_2 and HD molecules at low temperatures,” *Astron. Astrophys.* **589**, A105 (2016).
- [19] C. Jouvét and J. A. Beswick, “Fine structure electronic predissociation in van der waals molecules. i. theory,” *J. Chem. Phys.* **86**, 5500 (1987).
- [20] M. Quack and J. Troe, *Ber. Bunsenges. Phys. Chem* **78**, 240 (1974).
- [21] E. J. Rackham and F. Huarte-Larrañaga and D. E. Manolopoulos, “Coupled-channel statistical theory of the $N(^2D) + H_2$ and $O(^1D) + H_2$ insertion reactions,” *Chem. Phys. Lett.* **343**, 356 (2001).
- [22] E. J. Rackham, T. González-Lezana, and D. E. Manolopoulos, *J. Chem. Phys.* **119**, 12895 (2003).
- [23] M. H. Alexander, E. J. Rackham, and D. E. Manolopoulos, “Product multiplet branching in the $O(^1D) + H_2 \rightarrow OH(^2\Pi) + H$ reaction,” *J. Chem. Phys.* **121**, 5221 (2004).
- [24] T. González-Lezana, “Statistical quantum studies on insertion atom-diatom reactions,” *Int. Rev. Phys. Chem.* **26**, 29 (2007).
- [25] M. Konings and B. Desrousseaux and F. Lique and J. Loreau, “Benchmarking an improved statistical adiabatic channel model for competing inelastic and reactive processes,” *J. Chem. Phys.* **155**, 104302 (2021).
- [26] J. Mayneris and A. Saracibar and E. M. Goldfield and M. Gonzalez and E. García and S. K. Gray, “Theoretical study of the complex-forming $CH + H_2 \rightarrow CH_2 + H$ reaction,” *J. Phys. Chem. A* **110**, 5542 (2006).
- [27] H.-J. Werner, P. J. Knowles, G. Knizia, F. R. Manby, and M. Schütz, “Molpro: a general-purpose quantum chemistry program package,” *WIREs Comput Mol Sci* **2**, 242–253 (2012).
- [28] J. O. Hirschfelder and W. J. Meath, *The Nature of Intermolecular Forces*, Vol. 12 (Wiley, Chichester, 1967).
- [29] L. Velilla, B. Lepetit, A. Aguado, J. Beswick, and M. Paniagua, “The H_3^+ rovibrational spectrum revisited with a global electronic potential energy surface,” *J. Chem. Phys.* **129**, 084307 (2008).
- [30] A. Aguado, O. Roncero, and C. Sanz-Sanz, “Three states global fittings with improved long range: singlet and triplet states of H_3^+ ,” *PCCP* **23**, 7735 (2021).
- [31] S. Gómez-Carrasco, A. Aguado, M. Paniagua, and O. Roncero, “Coupled diabatic potential energy surfaces for studying the non-adiabatic dynamics at conical intersections in angular resolved photodetachment simulations of $OHF^- \rightarrow OHF + e^-$,” *J. Chem. Phys.* **125**, 164321 (2006).
- [32] NIST, “,” <https://webbook.nist.gov/chemistry/>, (2022).
- [33] D. Gerlich, “Reactive scattering of $N^+ + H_2$ and deuterated analogs: statistical calculation of cross sections and rate coefficients,” *J. Chem. Phys.* **90**, 3574 (1989).
- [34] P. Pechukas, J. C. Light, and C. Rankin, “Statistical theory of chemical kinetics: Application to neutral-atom-molecule reactions,” *J. Chem. Phys.* **44**, 794 (1966).
- [35] W. H. Miller, “Study of the statistical model for molecular collisions,” *J. Chem. Phys.* **52**, 543 (1970).
- [36] M. Quack and J. Troe, *Ber. Bunsenges. Phys. Chem* **79**, 170 (1975).
- [37] J. Troe, “Statistical adiabatic channel model for ion-molecule capture processes,” *J. Chem. Phys.* **87**, 2773 (1987).
- [38] T. González-Lezana, A. Aguado, M. Paniagua, and O. Roncero, “Quantum approaches for the insertion dynamics of the $H^+ + D_2$ and $D^+ + H_2$ reactive collisions,” *J. Chem. Phys.* **123**, 194309 (2005).
- [39] P.J. Chantry, “Doppler Broadening in Beam Experiments,” *J. Chem. Phys.* **55**, 2746 (1971).
- [40] A. Zanchet, O. Roncero, T. González-Lezana, A. Rodríguez-López, A. Aguado, C. Sanz-Sanz, and S. Gómez-Carrasco, “Differential cross sections and product rotational polarization in a+bc reactions using wave packet methods: $H^+ + D_2$ and $Li + HF$ examples,” *J. Phys. Chem. A* **113**, 14488 (2009).
- [41] O. Roncero, “Quantum wave packet program for triatomic systems,” <https://github.com/octavioroncero/madwave3> (2021).
- [42] O. Roncero, A. Aguado, and S. Gómez-Carrasco, “Radiative Processes in Astrophysical Molecules,” in *Gas-phase chemistry in space: from elementary particles to complex organic molecules*, AAS-IOP Astronomy, edited by Lique, F and Faure, A (IOP publishing ltd, Dirac house, Temple Back, Bristol BS1 6BE, England, 2019).
- [43] F. X. Gadéa, H. Berriche, O. Roncero, P. Villarreal, and G. Delgado-Barrio, “Nonradiative lifetimes for LiH in the a state using adiabatic and diabatic schemes,” *J. Chem. Phys.* **107**, 10515 (1997).
- [44] B. R. Johnson and R. D. Levine, “A new approach to non-adiabatic transitions in collision theory,” *Chem. Phys. Lett.* **13**, 168 (1972).
- [45] B. C. Garrett, M. J. Redmon, D. G. Truhlar, and C. F. Melius, “Ab initio treatment of electronically inelastic k+h collisions using a direct integration method for the solution of the coupled-channel scattering equations in electronically adiabatic representations,” *J. Chem. Phys.* **74**, 412 (1981).
- [46] B. Lepetit, J. M. Launay, and M. L. Dourneuf, “Quantum study of electronically non-adiabatic collinear reactions. i. hyperspherical description of the electronuclear dynamics,” *Chem. Phys.* **106**, 103 (1986).
- [47] D. W. Schwenke, D. G. Truhlar, and D. J. Kouri, “Propagation method for the solution of the arrangement-channel coupling equations for reactive scattering in three dimensions,” *J. Chem. Phys.* **86**, 2772 (1987).